Carbon Materials

Rapid Access to Ordered Mesoporous Carbons for Chemical Hydrogen Storage

Uiseok Jeong[+], HyeonJi Kim[+], Sreerangappa Ramesh, Nesibe A. Dogan, Sirinapa Wongwilawan, Sungsu Kang, Jungwon Park, Eun Seon Cho* and Cafer T. Yavuz*

Abstract: *Ordered mesoporous carbon materials offer robust network of organized pores for energy storage and catalysis applications, but suffer from time-consuming and intricate preparations hindering their widespread use. Here we report a new and rapid synthetic route for a N-doped ordered mesoporous carbon structure through a preferential heating of iron oxide nanoparticles by microwaves. A nanoporous covalent organic polymer is first formed in situ covering the hard templates of assembled nanoparticles, paving the way for a long-range order in a carbonaceous nanocomposite precursor. Upon removal of the template, a well-defined cubic mesoporous carbon structure was revealed. The ordered mesoporous carbon was used in solid state hydrogen storage as a host scaffold for NaAlH₄, where remarkable improvement in hydrogen desorption kinetics was observed. The state-of-the-art lowest activation energy of dehydrogenation as a single step was attributed to their ordered pore structure and N-doping effect.*

Introduction

Mesoporous carbon structures have been extensively studied owing to their potential in adsorption, separation, energy storage, drug delivery, catalysis with ordered and uniform pore channel, high surface area, and large pore volume.[1] Since the introduction of the highly ordered mesoporous carbon structure (CMK-1) by Ryoo's group,[2] various synthetic routes have been developed and reported by using templates[2,3] such as soft templating,[4] hard templating,[5] multiple templating[6] and in situ templating[7] methods. In addition, heteroatoms such as boron and nitrogen were incorporated into the pristine mesoporous carbons, for enabling their use in catalysis and electrochemistry. In particular, nitrogen-doped mesoporous carbon materials have attracted much attention owing to their exceptional performances in energy storage,[8] sensors,[9] and oxygen-reduction reaction (ORR)[5e,10] by increasing surface energy and reactivity. Because of the well-ordered pore structure and the tunable functionalities upon incorporation of heteroatoms, ordered mesoporous carbon materials are frequently employed as effective platforms for nanoconfinement in forming functional nanocomposites. For example, metal particles can be nanoconfined within such mesoporous carbons, leading to uniform and ordered hybrid structures with superior performances in energy storage or catalysis. In all such cases, the enhancements are mainly attributed to a controlled nanostructure, long range order, and interaction with doped heteroatoms of the ordered mesoporous carbons. The bottleneck for the widespread use of ordered mesoporous carbons is the lengthy procedures and steps required in conventional synthetic routes,[11] such as in evaporation-induced self-assembly.[4b] The methods often demand careful, time consuming manufacturing techniques, and prolonged heating to produce the mesoporous templates (Figure S1). A new approach is clearly needed, both in the assembly of hard templates and in heating profiles. In our quest of finding

[*] Dr. U. Jeong,[+] H. Kim,[+] S. Wongwilawan, Prof. E. S. Cho,
Prof. C. T. Yavuz
Department of Chemical and Biomolecular Engineering
Korea Advanced Institute of Science and Technology (KAIST)
Daejeon 34141 (Republic of Korea)
E-Mail: escho@kaist.ac.kr
        cafer.yavuz@kaust.edu.sa

Dr. S. Ramesh, Prof. C. T. Yavuz
Graduate School of EEWS
Korea Advanced Institute of Science and Technology (KAIST)
Daejeon 34141 (Republic of Korea)
E-Mail: cafer.yavuz@kaust.edu.sa

Dr. N. A. Dogan
Department of Bioproducts and Biosystems
School of Chemical Engineering, Aalto University
P.O. Box 16300, 00076 Aalto (Finland)

S. Kang, J. Park
School of Chemical and Biological Engineering and Institute of
Chemical Process, Seoul National University
Seoul 08826 (Republic of Korea)

J. Park
Center for Nanoparticle Research, Institute for Basic Science (IBS)
Seoul 08826 (Republic of Korea)

Prof. C. T. Yavuz
Advanced Membranes & Porous Materials Center, Physical Science
& Engineering (PSE), King Abdullah University of Science and
Technology (KAUST)
Thuwal 23955 (Saudi Arabia)
and
KAUST Catalysis Center, Physical Science & Engineering (PSE)
King Abdullah University of Science and Technology (KAUST)
Thuwal 23955 (Saudi Arabia)

[+] These authors contributed equally to this work.

Supporting information and the ORCID identification number(s) for
the author(s) of this article can be found under:
https://doi.org/10.1002/anie.202109215.

alternative paths, we envisioned that rapid self-assembly of uniform nanoparticles could alleviate the need for controlled assembly. And contrary to their ubiquitous use in organic synthesis,[12] we discovered that microwave heating has never been employed in ordering nanoparticle based hard templates for the mesoporous templating procedures. Existing literature mainly employs microwaves to facilitate rapid reaction and pyrolysis.[13]

One promising application for ordered mesoporous carbons is to be active hosts for hydrogen storage materials, where solid-state hydrogen storage techniques have become important for efficient and safe use of hydrogen as a future fuel. Among various hydrogen storage media, complex hydrides such as $NaAlH_4$ have been considered as leading materials on account of their high volumetric hydrogen storage capacities.[14] However, their practical use has been limited because of kinetic and thermodynamic barriers associated with hydrogen sorption. To resolve such drawbacks, complex hydrides have been introduced into porous scaffolds for nanoconfinement, leading to enhanced kinetics and thermodynamic characteristics for hydrogen sorption.[15] The size of confined complex hydride depends on the pore size of scaffold; thus, it is expected that a nanoconfinement effect on hydrogen sorption property of complex hydride is also determined by the pore structure of hosts. In addition, doping elements such as Ti, Ni, and N within mesoporous materials also play a catalytic role in hydrogen release and uptake of complex hydride due to an interfacial charge transfer and new structure formation.[16] In this respect, a controllable structure of mesoporous scaffold is critical to tailor hydrogen storage characteristics of confined complex hydrides.

In this work, we report a new and facile synthetic route for nitrogen-doped ordered mesoporous carbons using microwave preferential heating and show their use in effective nanoconfinement of $NaAlH_4$ for solid-state hydrogen storage, expecting both nanoscaling and nitrogen doping effects. We employ iron oxide (Fe_3O_4) nanoparticles as hard templates and self-assemble with polymeric precursors before a rapid microwave heating to form ordered nanocomposites. We call this new approach as preferential heating and assembly for nanoparticle templated ordered mesoporous materials (PHANTOM) method. The ordered mesoporous carbons as a confinement template provide a remarkable change in the dehydrogenation kinetics and associated mechanism of $NaAlH_4$ ascribed by the nanoporous structure and doped-nitrogen elements, making a great leap in chemical hydrogen storage.

Results and Discussion

Towards the goal of rapidly achieving ordered carbons, we first set out to attempt a new strategy to synthesize nitrogen embedded ordered mesoporous carbon structures by microwave irradiation (Scheme 1). By using the porous network framework of a covalent organic polymer (COP) as a rigid organic filler, we synthesized high nitrogen containing, hard templated carbon superstructure. For hard templates, we
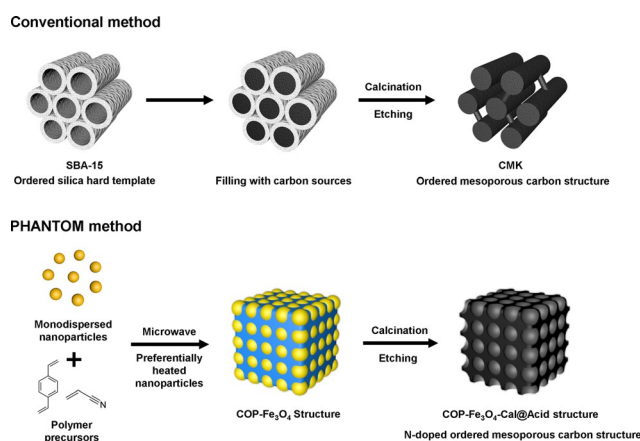
Scheme 1. Microwave heating for preferential assembly. Comparison of a conventional synthetic route with preferential heating and assembly for nanoparticle templated ordered mesoporous materials (PHANTOM) method.

employed easily synthesized, air stable iron oxide (Fe_3O_4) nanoparticles. Acrylonitrile (AN) is used as both carbon and nitrogen sources, as well as a linker to arrange nitrogen atoms in the carbon template.

We then prepared covalent organic polymer (COP-122) that is mixed with Fe_3O_4 nanoparticles as carbon precursors, but initially, it required more than one day of heating for complete crosslinking. And then almost all of the Fe_3O_4 nanoparticles were aggregated and phased out without properly encapsulating on the COP structures (Figure S2). This prompted us to exploit preferential heating through microwaves.

In a first attempt of its kind, COP-122-Fe_3O_4 nano-composites were successfully prepared in a dramatically decreased polymerization time (30 min) and with a highly ordered arrangement of Fe_3O_4 particles (Figures S3, S4). This confirmed our choice in developing a PHANTOM concept that utilizes hard templates being the primary thermal sources for superior packing mechanisms. In successive control experiments, both neat COP and COP-SiO_2 mixtures failed to make any product under the same microwave irradiation conditions (Table S1). We, therefore, concluded that 1) the porous network needs to be formed in situ, and 2) strong microwave absorbing iron oxide dispersed in non-aqueous media needed to stream-line packing in a biphasic system. Hence, we focused our study on a hexane dispersion of Fe_3O_4 nanoparticles with COP-122 forming and wrapping the nanoparticle assembly. To obtain an ordered array of hard templates, a monodispersed Fe_3O_4 solution was prepared (Figure S5, oleic acid coated Fe_3O_4 nanocrystals dispersed in hexane)[17] and mixed with covalent organic polymer precursors (COP-122)[18] in a Teflon tube, followed by heating at 90°C for 30 min in the microwave oven. The hydrophobic Fe_3O_4 nanoparticles promptly self-assembled on the polyol/ water surface without any treatment. As predicted, the microwave irradiation preferentially heated the iron oxide within the assembled clusters because of the significant difference in polarizability of the inorganic nanocrystalline media as opposed to flexible, organic, non-polar polymer

linkages. Once complete, the COP-Fe$_3$O$_4$ (CF) powder was calcined at various temperatures, followed by carbonization under Argon atmosphere, and treated with concentrated acid to remove Fe$_3$O$_4$ particles from the carbon structure. The CF-Calcination-Acid treatment structures (CFC-@XA) exhibited increased surface areas, uniform pore sizes and ordered mesoporous structures. We denoted these new ordered mesoporous carbons as CFC@XA, where „X" refers to the calcined temperature for pyrolysis of mesoporous carbon structures and „A" indicates the acid treatment.

Figure 1 shows structural properties of the synthesized nanomaterials. As evident from the TEM images, the uniform Fe$_3$O$_4$ nanoparticles carry their monodispersity to the nano-composites within the COP framework (Figure 1a, b). The challenge, however, was to achieve a reproducible calcination and digestion routine that preserve the long-range order. We prepared a series of samples by varying the synthetic conditions. First, the temperature of calcination was set from 500–800°C. Below 500°C, the calcination did not complete. In another series, we digested the embedded iron oxide prior to calcination (CFAC@X). All these samples were subjected to thorough analysis, particularly the porosity and crystallographic assessments (Figures S6–S11, S13–S15). We found that if calcination goes over 600°C, the order fails to hold and aggregation is inevitable. This is because the hard templating Fe$_3$O$_4$ nanoparticles tend to show sintering and Ostwald ripening, leading to polydisperse assemblies devoid of a long-range order. And if acid digestion precedes the calcination,

then the pores collapse and give very low porosities with clear lack of uniformity (Figures S12–15). The extensive TEM and SEM imaging on these samples along with TEM-EDX mapping confirmed the observations (Figures S16, 17). The CF sample that was calcined at 500°C(CFC@500A), however, showed ordered and uniform mesoporous carbon structure without any deleterious signs from calcination or acid digestion (Figure 1c, d).

The mesoporous properties of CFC@XA structures were investigated with Brunauer–Emmett–Teller (BET) N$_2$ isotherms and pore size distributions were obtained using both Barrett, Joyner and Halenda (BJH) and nonlocal density functional theory (NLDFT) methods (Figure 1e, f and S18). In particular, the N$_2$ adsorption–desorption isotherms of CFC@500A demonstrates IUPAC type IV BET curve with a H2 hysteresis loop,[19] indicating the uniform microporous and mesoporous structure with bottle type of pore geometries. The BET surface areas, total pore volumes, average pore sizes of all the synthesized structures are summarized in Table 1. The small portion of micropore volume originates from the COP-122 structure, and the large amount of increased total pore volume is ascribed by the uniform mesoporous structure from the ordered Fe$_3$O$_4$ nanoparticle templated voids. Both BET surface area and total pore volume substantially increased for CFC@500A, compared to the initial CF structure (32 vs. 478 m^{2}g^{-1} and 0.1311 vs. 0.6845 cm^{3}g^{-1}, respectively). On the other hand, the surface area of CFC@600–800A structures decreased to 244, 199 and
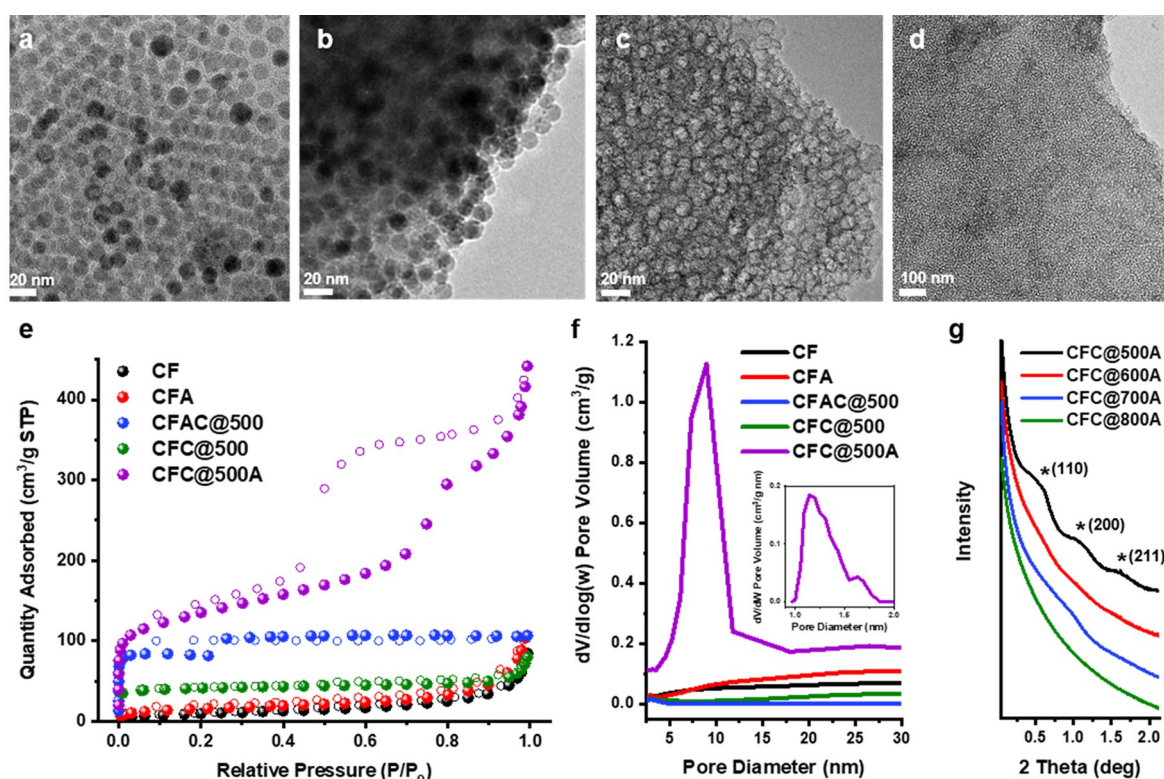

Figure 1. Physical properties of COP-Fe$_3$O$_4$ (CF) structures. TEM images of a) monodispersed Fe$_3$O$_4$ nanoparticles in hexane, b) as synthesized CF particles, and c),d) CFC@500A samples. e),f) N$_2$ adsorption-desorption isotherms (77 K) and the corresponding pore size distribution of synthesized samples. g) SAXRD patterns reflecting long range of mesopores.

Table 1: Comparison table of physical properties of obtained mesoporous carbon structures.

Sample	S_{BET}[a] [m²g⁻¹]	S_{mic}[b] [m²g⁻¹]	V_t[c] [cm³g⁻¹]	V_{mic}[d] [m³g⁻¹]	D_p[e] [nm]	C[f] [wt%]	N[f] [wt%]	O[f] [wt%]	H[f] [wt%]	CO₂ uptake[g] [mmol g⁻¹]
CF	32	–	0.1311	–	9.08	48.19	2.05	17.42	4.52	0.48
CFA	53	4	0.1611	0.0030	9.11	82.46	3.22	2.98	7.60	0.81
CFAC@500	344	79	0.1654	0.0220	9.10	88.45	1.60	1.28	3.70	2.12
CFC@500A	478	234	0.6845	0.1052	8.95	74.63	1.60	5.93	3.07	1.90
CFC@600A	244	83	0.5211	0.0379	8.94	86.85	0.80	1.93	1.53	1.71
CFC@700A	199	114	0.6357	0.0461	8.82	88.34	0.38	0.86	1.02	0.95
CFC@800A	289	98	0.4259	0.0476	8.94	88.76	0.24	1.01	0.53	1.24

[a] BET specific surface areas evaluated in p/po from 0.05 to 0.25. [b] Micropore surface areas calculated through the t-plot method. [c] Total pore volumes estimated based on the volume absorbed at p/po of ca. 0.995. [d] Micropore volumes calculated through the t-plot method. [e] pore size derived from the adsorption branches of the isotherms by using the BJH method. [f] Chemical composition data from elemental analysis (C,N,O,H). The left-over inorganic solids constitute the remaining balance of the elemental content. In higher temperature annealed samples, the inorganics tend to sinter and subsequently be etched out more effectively. [g] CO₂ uptake capacity at 273 K and 1.0 bar.

289 m²g⁻¹, respectively. Furthermore, only CFC@500A presented a strongly concentrated and increased BJH pore size distribution peak at 8.95 nm (Figure 1 f and S18).

The transformation of CFC@XA structures during the synthetic process were further examined to understand the chemical nature of the mesoporous materials. The crystalline structure of Fe_3O_4 particles was converted into pure Fe and Fe_3C upon calcination at the temperature higher than 600°C as shown in the X-ray diffraction (XRD) pattern (Figure S19). Furthermore, even after acid treatment these high temperature samples still contained large amount of Fe residue in the carbon structure as a carbide along with graphite, except in the ordered sample CFC@500A. In the small-angle X-ray diffraction (SAXRD) measurement (Figure 1g), the CFC@500A shows strong peaks at 0.55°, 1.10° and 1.65°, which correspond to (110), (200), (211) planes, respectively, of the *Im3̄m* space group, supporting that the obtained ordered mesoporous carbon consists of 3D cubic crystalline structure.[20]

In the Raman spectra of CFC@500 and CFC@500A (Figure S20), two bands are observed clearly at 1345 and 1595 cm⁻¹, which explains the C−C single bonds between sp³ hybridized carbon atoms and in-plane displacement of the sp² bonded carbons, respectively. It supports that the carbon structures of CFC@500A sample are well preserved during the acid treatment. Furthermore, all the prepared samples possess the thermal stability up to 400°C in air, while the carbons calcined at higher temperatures tend to be more stable, as shown in thermogravimetric analysis (TGA) (Figure S21). The chemical environment and structure of each CFC@XA sample were further investigated by elemental analysis (EA) and X-ray photoelectron spectroscopy (XPS). The EA data show the trend of atomic ratio in the samples depending on the calcined temperature. When the pyrolysis temperature increased from 500 to 800°C, the content of nitrogen in the structure decreased from 1.6% to 0.24% (Table 1). The elevated temperatures clearly foster decomposition through nitric oxides, bringing further disordering in the otherwise ordered mesoporous networks. In the XPS analysis, three distinct nitrogen functional groups associated with carbon, which include pyridinic, pyrrolic, and graphitic

nitrogen, were detected, along with nitrate for CFC@500A (Figure S22).

The N-embedded CFC@A mesoporous carbon structures revealed enhanced CO₂ adsorption capacity (Figure S23), a clear evidence for the high loading of nitrogen throughout the mesoporous domain. For our main purpose of metal hydride dehydrogenation, it is crucial that we sustain a high heteroatom content for a catalytic effect. In general, CO₂ uptake capacity is dependent on the surface area, heteroatom content, and morphology of the adsorbent. However, in the adsorption results (Table 1), CFAC@500 sample showed the highest CO₂ uptake even though the pore sizes shrunk after calcination. This is likely due to the physical property of the transformed and shriveled CFAC@500 which lost its mesoporous property. At the 273 K, CFC@XA structure showed higher CO₂ uptake of 1.90, 1.71, 0.95 and 1.24 mmol g⁻¹ than original CF structure (0.48 mmol g⁻¹, Table 1). CFC@500A showed four times increased CO₂ adsorption capacity than CF. The other CFC@A structures showed decreasing CO₂ uptake along with the lower embedded nitrogen content. Furthermore, we performed gas adsorption and desorption test at 273, 298 and 323 K (CO₂, N₂, CH₄) to check the gas selectivity of CFC@A structures (Figures S23–25). By using the ideal adsorbed solution theory (IAST), CFC@500A (8–57) and CFC@600A (44–48) demonstrated larger CO₂/ N₂ (15:85) selectivity than others at 1 bar (Figure S26 and Table S2). To reveal the surface affinity of the CFC@A structures to CO₂, the isosteric heat of adsorption (Q_{st}) was calculated by using the Clausius–Clapeyron equation (Figure S27). The Q_{st} value at the initial adsorption stage mainly reflects the interaction strength between CO₂ and the adsorbent.[21] CFC@500A exhibits higher initial Q_{st} value of 32.94 kJ mol⁻¹ than the CFC@600, 700, 800A, where Q_{st} are 29.27, 11.89 and 25.41 kJ mol⁻¹, respectively.

The CFC@500A is employed as a nanoconfinement scaffold for NaAlH₄, expecting both nanoscaling and catalytic effects on hydrogen storage properties from the well-ordered pore structure and uniform N-doping, respectively. A nanocomposite of NaAlH₄ and CFC@500A (CFC@NaAlH₄) was synthesized to examine the influence of mesoporous carbon scaffolds on hydrogen storage property of confined NaAlH₄. Also, a simple physical mixture of NaAlH₄ and CFC@500A
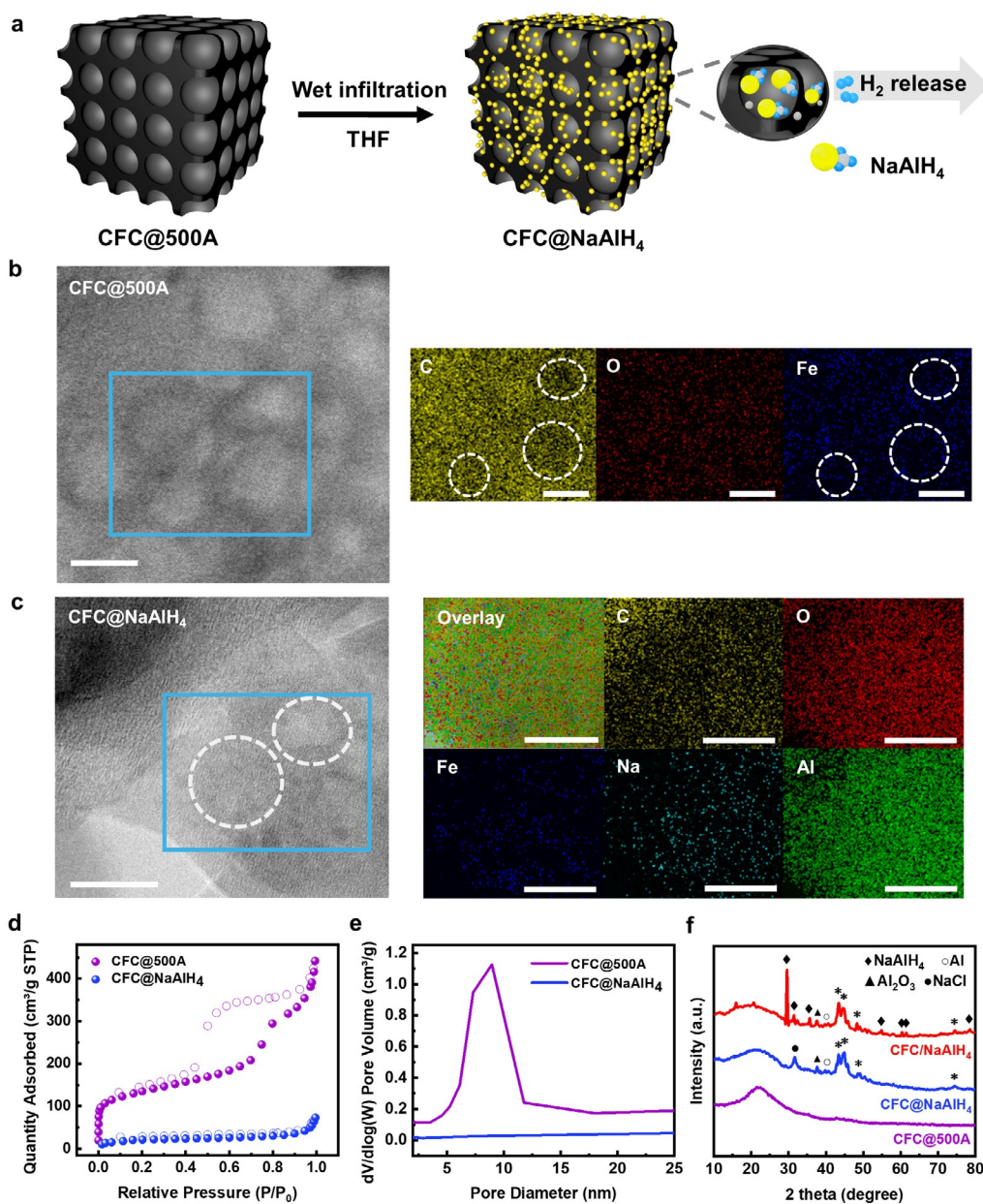
Figure 2. Nanoconfinement of NaAlH₄ in CFC@500A. a) Wet infiltration of NaAlH₄ into CFC@500A (CFC@NaAlH₄). STEM-EDS images of b) CFC@500A and c) CFC@NaAlH₄ in which the white circles indicate the nanopores of CFC@500A (all scale bars are 10 nm). d) N₂ adsorption–desorption isotherms (77 K) of as-prepared samples and e) the pore size distribution of CFC@NaAlH₄ compared with CFC@500A. f) PXRD patterns of CFC@500A, CFC@NaAlH₄, and CFC/NaAlH₄ (*mark represents the peaks from stainless steel sample holder which was used to prevent air exposure of the samples).

(CFC/NaAlH₄) was prepared as a control sample to scrutinize the nanoconfinement effect (further details can be found in the Experimental Procedures in the Supporting Information). Figure 2a represents a scheme to illustrate that both 1–2 nm and 8–10 nm pores were filled by nanosized NaAlH₄ through wet infiltration using THF as a solvent. The homogeneous pores which have both 1–2 nm and 8–10 nm sizes were formed by chemical bonding within polymer precursors and Fe₃O₄ nanoparticles, respectively. To demonstrate the incorporated NaAlH₄ within nanopores of carbon scaffold, bright-field scanning transmission electron microscopy–energy-dispersive X-ray spectroscopy (BF-STEM-EDS) was implemented for

pristine CFC@500A and CFC@NaAlH₄ (Figure 2b, c). According to CFC@500A STEM-EDS, the brighter regions with near-circular shapes represent nanopores where less carbon tends to be detected in EDS mapping, as indicated by white circles (Figure 2b). Also, the residual Fe₃O₄ particles were identified mainly around the pores, not inside the pores of CFC@500A supported by Fe mapping. Similarly, for CFC@NaAlH₄, carbon is uniformly distributed and less detected on nanopores specified, and Fe₃O₄ particles were also found outside the pores as shown in STEM-EDS measurements of CFC@NaAlH₄ (Figure 2c). However, Na and Al were newly detected in identical regions, while the

intensity of Na mapping was lower than Al due to electron beam damage of Na.[22] Al_xO_y was likely formed by air exposure during the specimen transfer process to the TEM. Notably, Na was identified where carbon mapping showed weak intensity which implies nanopores, demonstrating the presence of infiltrated $NaAlH_4$ into CFC@500A pores. The surface area of CFC@$NaAlH_4$ significantly decreases, compared to that of the neat CFC@500A, of which values are $478\ m^2 g^{-1}$ and $80\ m^2 g^{-1}$, respectively, from BET isotherms (Figure 2 d, e). Also, no significant pore volume was identified, as opposed to the carbon template, CFC@500A, in which case it was measured as $0.6845\ cm^3 g^{-1}$ (Table 1). This result indicates that $NaAlH_4$ was confined in and blocked the CFC@500A nanopores. Powder X-ray Diffraction measurement (PXRD) was employed to confirm the infiltration of $NaAlH_4$. As shown in Figure 2 f, a broad peak at around 20 degree was attributed to the porous carbon framework and maintained for both CFC/$NaAlH_4$ and CFC@$NaAlH_4$. Some impurities such as NaCl and aluminum oxide were also

detected at 31, 38 degrees owing to high reactivity of $NaAlH_4$ and aluminum oxidation. The typical crystalline $NaAlH_4$ peaks were not detected in CFC@$NaAlH_4$ whereas the physical mixture, CFC/$NaAlH_4$, showed crystalline $NaAlH_4$ XRD peaks. It suggests that $NaAlH_4$ is successfully incorporated into nano-sized pores of the CFC@500A during the wet infiltration, in which case it exists as nano-crystallites or an amorphous form.[23] The existence of intact $NaAlH_4$ was further identified by the FTIR spectrum (Figure S28). Although the original CFC@500A peaks were coincided, AlH_4^- stretching and bending peaks at 880 and $1670\ cm^{-1}$ were shown in CFC@ $NaAlH_4$, meaning that $NaAlH_4$ was incorporated and undamaged after the infiltration process. Therefore, it can be deduced that $NaAlH_4$ particles were successfully nanoconfined within the pore of CFC@500A.

To examine the dehydrogenation kinetics of CFC-@$NaAlH_4$, temperature-programmed desorption–mass spectrometry (TPD-MS) was implemented under Ar atmosphere at 1 bar. It is known that hydrogen is released from bulk
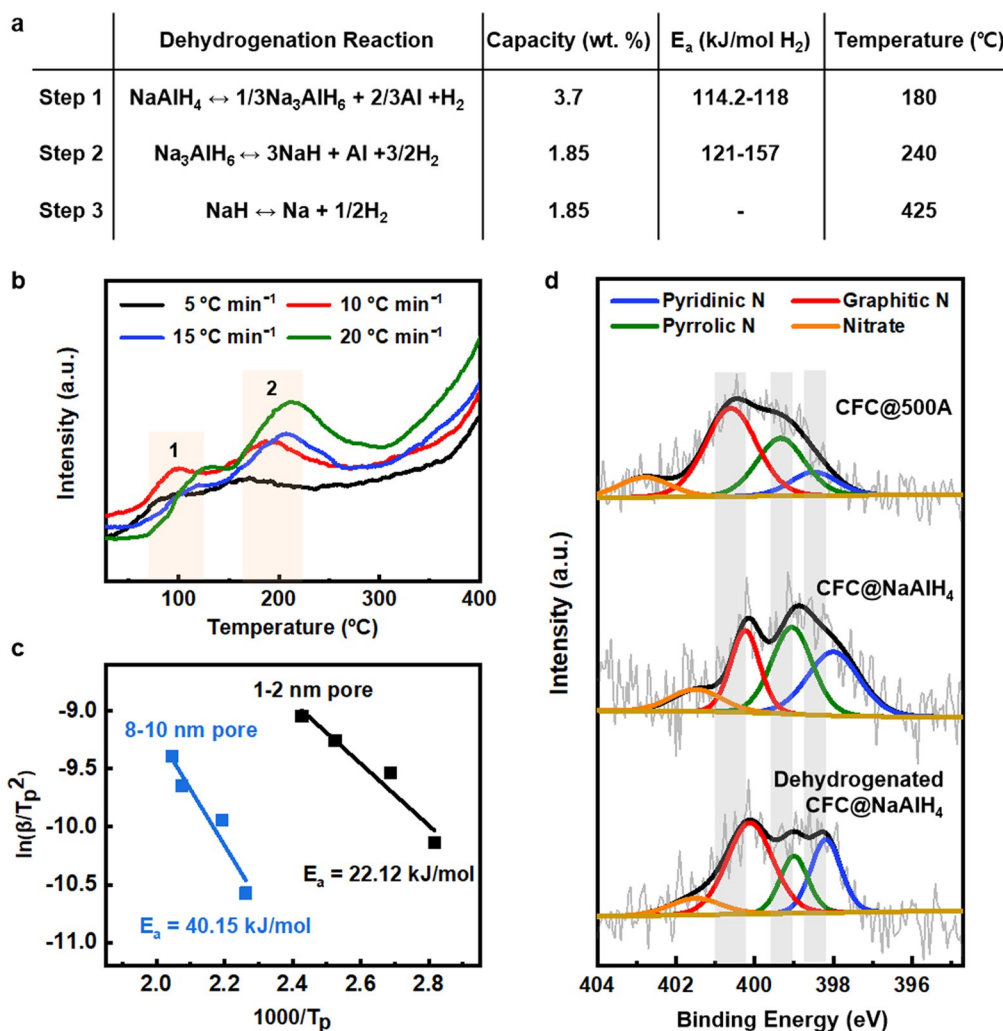

	Dehydrogenation Reaction	Capacity (wt. %)	E_a (kJ/mol H_2)	Temperature (°C)
Step 1	$NaAlH_4 \leftrightarrow 1/3Na_3AlH_6 + 2/3Al + H_2$	3.7	114.2-118	180
Step 2	$Na_3AlH_6 \leftrightarrow 3NaH + Al + 3/2H_2$	1.85	121-157	240
Step 3	$NaH \leftrightarrow Na + 1/2H_2$	1.85	-	425

Figure 3. Dehydrogenation mechanism analysis of CFC@$NaAlH_4$. a) Three steps of dehydrogenation reaction and corresponding hydrogen capacity, activation energy of dehydrogenation, and desorption temperature for bulk $NaAlH_4$. (The activation energy of bulk $NaAlH_4$ and Na_3AlH_6 is obtained from the literature.[26]). b) TPD-MS of desorbed hydrogen from CFC@$NaAlH_4$ while varying the heating rates (5, 10, 15, 20 °C min⁻¹). c) Kissinger plots of CFC@$NaAlH_4$ based on TPD-MS data. d) N 1s XPS spectra of CFC@500A, CFC@$NaAlH_4$, and dehydrogenated CFC@$NaAlH_4$.

NaAlH₄ in a stepwise procedure (Figure 3a). In their bulk form without nanoscaling and confinement into carbon scaffolds, the kinetic barrier for dehydrogenation is significantly high, beyond the bounds of practical application. To evaluate the effect of the mesoporous carbon scaffolds, the dehydrogenation kinetics of CFC@NaAlH₄ was investigated while varying the heating rate as 5, 10, 15, and 20°C min⁻¹ (Figure 3b). At 5°C min⁻¹ heating rate, CFC@ NaAlH₄ starts to desorb hydrogen below 50°C and the peak temperature is about 80°C, reduced by 100°C compared with bulk NaAlH₄. During desorption measurement, hydrogen is also detected at higher temperatures above 300°C, presumably not released from the confined NaAlH₄ based on its desorption behavior. It is speculated that oxygen in the remained THF can form Al₂O₃ nanoclusters, leading to release hydrogen and other volatile gases by a redox reaction.[23a,24] In contrast with the three steps of dehydrogenation in bulk NaAlH₄, the two distinguishable peaks were observed for dehydrogenation of CFC@NaAlH₄, as indicated in Figure 3b. To confirm the dehydrogenation mechanism shown as two isolated peaks, the PXRD patterns of CFC@NaAlH₄ dehydrogenated at 120°C, in the middle of two desorption peaks, was measured (Figure S29). Such partially dehydrogenated CFC@NaAlH₄ showed several peaks associated with NaH, NaCl, Al₂O₃, and Al particles. Specifically, Al particles exist with NaH as products of the dehydrogenation process, while NaCl was formed by a reaction between NaAlH₄ and Cl from the calcination process. It is noticeable that NaH was uncovered in the dehydrogenated sample at 120°C because NaH formation is not feasible during the dehydrogenation process at such a lower temperature. In contrast, bulk NaAlH₄ dehydrogenated at 120°C maintained its crystalline structure as pristine NaAlH₄, not forming any products like Na₃AlH₆ and NaH. It has been reported that Na₃AlH₆ nanoparticles are seldom formed when the particle size decreases due to high surface energy of Na₃AlH₆.[25] As revealed in a phase diagram and reaction map, the altered reaction pathway from two-step decomposition (Reaction I and IIa) to one-step decomposition (Reaction III) with direct NaH formation was demonstrated as the NaAlH₄ particle size decreases (Figure S30). Thus, the formation of NaH at 120°C for CFC@ NaAlH₄ confirms the alteration of the thermodynamic pathway of hydrogen release for NaAlH₄ as a result of nanoconfinement. Accordingly, each peak in TPD-MS measurement is in agreement with one step dehydrogenation procedure, simply separated by two different sized pores: 1–2 nm and 8–10 nm.

The activation energy of hydrogen desorption for CFC@NaAlH₄ was determined by the Kissinger method[27] using the peak temperatures dependent on each heating rate (Figure 3c) (the details are described in Supporting Information). The activation energies for dehydrogenation of confined NaAlH₄ in 1–2 nm and 8–10 nm pores were calculated as 22.12 kJ mol⁻¹ H₂ and 40.15 kJ mol⁻¹ H₂, respectively. To the best of our knowledge, the CFC@NaAlH₄ showed the lowest dehydrogenation activation energy among other reported NaAlH₄-based materials including other various transition metal catalyst doped NaAlH₄ (Table S3). Since some NaAlH₄ would react with nitrogen or oxygen contained

in CFC@500A, the hydrogen capacity of infiltrated NaAlH₄ was approximately 3 wt.% which is lower than the theoretical value. However, with a significant reduction in the activation energy, CFC@NaAlH₄ exhibited the unprecedently lower temperature for hydrogen release.

Such noticeable advancement in kinetics can be attributed to the synergistic effect of nanoconfinement and N-doping of CFC@500A. In general, the nanoconfinement of NaAlH₄ leads to the reduction in diffusion length of hydrogen, surface energy increment, and additional electronic interactions with the scaffold, which eventually contributes to the enhanced dehydrogenation kinetics or thermodynamic pathway alteration.[15a,28] Upon nanoscaling, NaAlH₄ directly decomposes to NaH through the modified reaction pathway where no unstable intermediate, Na₃AlH₆ is produced during dehydrogenation as opposed to the case of bulk NaAlH₄ (Figure 3a).[25,29] Furthermore, it is known that nanosized NaAlH₄ is considerably influenced by electronegative carbon scaffolds through electronic interactions.[30] Since the stability of NaAlH₄ is derived from ionic strength between Na⁺ and AlH₄⁻ and covalent bonding of Al−H, NaAlH₄ can be easily disintegrated into Na⁺ and AlH₄⁻ when the carbon scaffold provides negative charge to NaAlH₄. It generates AlH₃ vacancy and promotes the diffusion of hydrogen through rapid transformation in hydride structure, which results in hydrogen release under mild condition. Therefore, we conclude that the nanoconfinement of NaAlH₄ into CFC@500A pores lowered both onset temperature and activation energy value for hydrogen desorption, ascribed by nanosizing and electronic interaction with carbon framework. Another attribute to the improved dehydrogenation kinetics of CFC@NaAlH₄ is the doping effect originated from an N-embedded structure of carbon scaffold. The previous studies demonstrated that the addition of nitrogen doped species into complex hydrides decreased the hydrogen release energy and facilitated the removal of hydrogen as a result of electronic charge transfer.[16c,31] The interaction between the nitrogen in CFC@500A and the infiltrated NaAlH₄ was confirmed from N 1s XPS (Figure 3d). The shift toward lower binding energy suggests that the incorporated NaAlH₄ particles closely interact and reduce the doped nitrogen. Also, the relative intensity of graphitic nitrogen was reduced, while that of pyridinic and pyrrolic nitrogen increased after NaAlH₄ infiltration, indicating the increment in the relative content of Lewis base for NaAlH₄ (Table S4).[16c] The charge donation from nitrogen was further investigated with the dehydrogenated CFC@NaAlH₄, in which case the relative content of pyridinic nitrogen decreased and its peak was shifted to higher binding energy (Figure 3d and Table S4). It suggests that the pyridinic nitrogen acts as a Lewis base to provide negative charges to Na⁺ during hydrogen release reactions. Thus, the destabilization of NaAlH₄ induces the fast formation of AlH₃ through negative charge transfer from nitrogen to NaAlH₄, resulting in NaAlH₄ decomposition at lower temperatures.

Conclusion

We report a new and facile synthetic route for N-doped ordered mesoporous carbon structure by using microwave preferential heating and assembly, and its application as a functional scaffold for solid-state hydrogen storage materials. The rapid, selective heating of the iron oxide nanoparticles forces the nanoporous polymer to form around and wrap the nanoparticles, leading to a precursor with long range order. Upon optimizing the calcination and digestion procedures, we showed that ordered mesoporous carbons can be achieved. These ordered nanopores acted as an effective platform of $NaAlH_4$ for feasible solid-state hydrogen storage, where the synergistic effect of nanoconfinement and doped-nitrogen as a catalytic function was demonstrated. Furthermore, the lowest activation energy of $NaAlH_4$ dehydrogenation with the altered reaction pathway was presented. Together with the rapid and selective formation of the ordered porous structure through microwave heating, the nanoconfinement strategies offer tremendous potential in hydrogen storage or heterogeneous catalysis. We expect a substantial development in PHANTOM based mesoporous materials and their applications in energy and environment.

Acknowledgements

Conflict of Interest

The authors declare no conflict of interest.

Stichwörter: hard template synthesis · hydrogen storage · microwave heating · nanoconfinement · nitrogen doped carbon

[1] a) M. R. Benzigar, S. N. Talapaneni, S. Joseph, K. Ramadass, G. Singh, J. Scaranto, U. Ravon, K. Al-Bahily, A. Vinu, *Chem. Soc. Rev.* **2018**, *47*, 2680–2721; b) J. P. Paraknowitsch, A. Thomas, *Energy Environ. Sci.* **2013**, *6*, 2839–2855; c) J. T. Zhang, Z. H. Xia, L. M. Dai, *Sci. Adv.* **2015**, *1*, e1500564; d) P. F. Zhang, J. S. Zhang, S. Dai, *Chem. Eur. J.* **2017**, *23*, 1986–1998; e) A. H. Lu, G. P. Hao, Q. Sun, *Angew. Chem. Int. Ed.* **2013**, *52*, 7930–7932; *Angew. Chem.* **2013**, *125*, 8086–8087; f) Z. A. Qiao, B. K. Guo, A. J. Binder, J. H. Chen, G. M. Veith, S. Dai, *Nano Lett.* **2013**, *13*, 207–212; g) S. Wang, W. C. Li, G. P. Hao, Y. Hao, Q. Sun, X. Q. Zhang, A. H. Lu, *J. Am. Chem. Soc.* **2011**, *133*, 15304–15307.

[2] R. Ryoo, S. H. Joo, S. Jun, *J. Phys. Chem. B* **1999**, *103*, 7743–7746.

[3] a) J. Lee, S. Han, T. Hyeon, *J. Mater. Chem.* **2004**, *14*, 478–486; b) J. Lee, S. Yoon, T. Hyeon, S. M. Oh, K. B. Kim, *Chem. Commun.* **1999**, 2177–2178; c) R. Ryoo, S. H. Joo, M. Kruk, M. Jaroniec, *Adv. Mater.* **2001**, *13*, 677–681; d) R. Ryoo, I. S. Park, S. Jun, C. W. Lee, M. Kruk, M. Jaroniec, *J. Am. Chem. Soc.* **2001**, *123*, 1650–1657.

[4] a) D. C. Wu, F. Xu, B. Sun, R. W. Fu, H. K. He, K. Matyjaszewski, *Chem. Rev.* **2012**, *112*, 3959–4015; b) Y. H. Deng, J. Wei, Z. K. Sun, D. Y. Zhao, *Chem. Soc. Rev.* **2013**, *42*, 4054–4070; c) S. Ghosh, N. A. Kouame, L. Ramos, S. Remita, A. Dazzi, A. Deniset-Besseau, P. Beaunier, F. Goubard, P. H. Aubert, H. Remita, *Nat. Mater.* **2015**, *14*, 505–511; d) R. Y. Zhang, Y. J. Du, D. Li, D. K. Shen, J. P. Yang, Z. P. Guo, H. K. Liu, A. A. Elzatahry, D. Y. Zhao, *Adv. Mater.* **2014**, *26*, 6749–6755; e) J. Liu, T. Y. Yang, D. W. Wang, G. Q. M. Lu, D. Y. Zhao, S. Z. Qiao, *Nat. Commun.* **2013**, *4*, 2798; f) J. Wei, D. D. Zhou, Z. K. Sun, Y. H. Deng, Y. Y. Xia, D. Y. Zhao, *Adv. Funct. Mater.* **2013**, *23*, 2322–2328.

[5] a) X. L. Ji, K. T. Lee, R. Holden, L. Zhang, J. J. Zhang, G. A. Botton, M. Couillard, L. F. Nazar, *Nat. Chem.* **2010**, *2*, 286–293; b) H. W. Liang, W. Wei, Z. S. Wu, X. L. Feng, K. Mullen, *J. Am. Chem. Soc.* **2013**, *135*, 16002–16005; c) H. W. Liang, X. D. Zhuang, S. Bruller, X. L. Feng, K. Mullen, *Nat. Commun.* **2014**, *5*, 4973; d) T. Q. Lin, I. W. Chen, F. X. Liu, C. Y. Yang, H. Bi, F. F. Xu, F. Q. Huang, *Science* **2015**, *350*, 1508–1513; e) R. L. Liu, D. Q. Wu, X. L. Feng, K. Mullen, *Angew. Chem. Int. Ed.* **2010**, *49*, 2565–2569; *Angew. Chem.* **2010**, *122*, 2619–2623; f) W. H. Niu, L. G. Li, X. J. Liu, N. Wang, J. Liu, W. J. Zhou, Z. H. Tang, S. W. Chen, *J. Am. Chem. Soc.* **2015**, *137*, 5555–5562; g) X. C. Wang, K. Maeda, X. F. Chen, K. Takanabe, K. Domen, Y. D. Hou, X. Z. Fu, M. Antonietti, *J. Am. Chem. Soc.* **2009**, *131*, 1680–1681.

[6] a) Z. Y. Guo, D. D. Zhou, X. L. Dong, Z. J. Qiu, Y. G. Wang, Y. Y. Xia, *Adv. Mater.* **2013**, *25*, 5668–5672; b) G. Li, J. H. Sun, W. P. Hou, S. D. Jiang, Y. Huang, J. X. Geng, *Nat. Commun.* **2016**, *7*, 10601; c) H. J. Liu, J. Wang, C. X. Wang, Y. Y. Xia, *Adv. Energy Mater.* **2011**, *1*, 1101–1108; d) M. Oschatz, L. Borchardt, K. Pinkert, S. Thieme, M. R. Lohe, C. Hoffmann, M. Benusch, F. M. Wisser, C. Ziegler, L. Giebeler, M. H. Rummeli, J. Eckert, A. Eychmuller, S. Kaskel, *Adv. Energy Mater.* **2014**, *4*, 1300645; e) L. Qie, W. M. Chen, H. H. Xu, X. Q. Xiong, Y. Jiang, F. Zou, X. L. Hu, Y. Xin, Z. L. Zhang, Y. H. Huang, *Energy Environ. Sci.* **2013**, *6*, 2497–2504; f) Z. S. Wu, Y. Sun, Y. Z. Tan, S. B. Yang, X. L. Feng, K. Mullen, *J. Am. Chem. Soc.* **2012**, *134*, 19532–19535.

[7] a) W. Li, F. Zhang, Y. Q. Dou, Z. X. Wu, H. J. Liu, X. F. Qian, D. Gu, Y. Y. Xia, B. Tu, D. Y. Zhao, *Adv. Energy Mater.* **2011**, *1*, 382–386; b) Z. Li, Z. W. Xu, X. H. Tan, H. L. Wang, C. M. B. Holt, T. Stephenson, B. C. Olsen, D. Mitlin, *Energy Environ. Sci.* **2013**, *6*, 871–878; c) M. W. Schulze, L. D. McIntosh, M. A. Hillmyer, T. P. Lodge, *Nano Lett.* **2014**, *14*, 122–126.

[8] X. W. Zhong, Y. Z. Li, L. Z. Zhang, J. Tang, X. N. Li, C. Liu, M. M. Shao, Z. G. Lu, H. Pan, B. M. Xu, *ACS Appl. Mater. Interfaces* **2019**, *11*, 2970–2977.

[9] J. Zhou, B. Yang, Z. J. Li, L. C. Lei, X. W. Zhang, *Ind. Eng. Chem. Res.* **2015**, *54*, 2329–2338.

[10] W. Yang, T. P. Fellinger, M. Antonietti, *J. Am. Chem. Soc.* **2011**, *133*, 206–209.

[11] P. Zhang, L. Wang, S. Yang, J. A. Schott, X. Liu, S. M. Mahurin, C. Huang, Y. Zhang, P. F. Fulvio, M. F. Chisholm, S. Dai, *Nat. Commun.* **2017**, *8*, 15020.

[12] C. O. Kappe, *Angew. Chem. Int. Ed.* **2004**, *43*, 6250–6284; *Angew. Chem.* **2004**, *116*, 6408–6443.

[13] a) H. I. Lee, J. H. Kim, S. H. Joo, H. Chang, D. Seung, O.-S. Joo, D. J. Suh, W.-S. Ahn, C. Pak, J. M. Kim, *Carbon* **2007**, *45*, 2851–2854; b) K. S. Lakhi, W. S. Cha, J.-H. Choy, M. Al-Ejji, A. M. Abdullah, A. M. Al-Enizi, A. Vinu, *Microporous Mesoporous*

Mater. **2016**, *233*, 44–52; c) U. B. Nasini, V. G. Bairi, S. K. Ramasahayam, S. E. Bourdo, T. Viswanathan, A. U. Shaikh, *J. Power Sources* **2014**, *250*, 257–265.

[14] a) L. Schlapbach, A. Züttel, *Nature* **2001**, *414*, 353–358; b) S.-i. Orimo, Y. Nakamori, J. R. Eliseo, A. Züttel, C. M. Jensen, *Chem. Rev.* **2007**, *107*, 4111–4132.

[15] a) C. P. Baldé, B. P. C. Hereijgers, J. H. Bitter, K. P. de Jong, *Angew. Chem. Int. Ed.* **2006**, *45*, 3501–3503; *Angew. Chem.* **2006**, *118*, 3581–3583; b) X. Liu, D. Peaslee, C. Z. Jost, E. H. Majzoub, *J. Phys. Chem. C* **2010**, *114*, 14036–14041; c) P. Adelhelm, P. E. de Jongh, *J. Mater. Chem.* **2011**, *21*, 2417–2427.

[16] a) R. Xiong, G. Sang, G. Zhang, X. Yan, P. Li, Y. Yao, D. Luo, C. a. Chen, T. Tang, *Int. J. Hydrogen Energy* **2017**, *42*, 6088–6095; b) X. Zhang, Z. Ren, Y. Lu, J. Yao, M. Gao, Y. Liu, H. Pan, *ACS Appl. Mater. Interfaces* **2018**, *10*, 15767–15777; c) C. L. Carr, W. Jayawardana, H. Zou, J. L. White, F. El Gabaly, M. S. Conradi, V. Stavila, M. D. Allendorf, E. H. Majzoub, *Chem. Mater.* **2018**, *30*, 2930–2938.

[17] C. T. Yavuz, J. T. Mayo, W. W. Yu, A. Prakash, J. C. Falkner, S. Yean, L. L. Cong, H. J. Shipley, A. Kan, M. Tomson, D. Natelson, V. L. Colvin, *Science* **2006**, *314*, 964–967.

[18] N. A. Dogan, E. Ozdemir, C. T. Yavuz, *ChemSusChem* **2017**, *10*, 2130–2134.

[19] a) J. C. P. Broekhoff, W. P. Vanbeek, *J. Chem. Soc. Faraday Trans. 1* **1979**, *75*, 42–55; b) K. S. W. Sing, D. H. Everett, R. A. W. Haul, L. Moscou, R. A. Pierotti, J. Rouquerol, T. Siemieniewska, *Pure Appl. Chem.* **1985**, *57*, 603–619; c) S. Lowell, J. E. Shields, M. A. Thomas, M. Thommes in *Characterization of porous solids and powders : surface area, pore size, and density*, Springer, Dordrecht, **2006**, pp. 347.

[20] a) K. Saito, Y. Yamamura, Y. Miwa, S. Kutsumizu, *Phys. Chem. Chem. Phys.* **2016**, *18*, 3280–3284; b) Y. Meng, D. Gu, F. Q. Zhang, Y. F. Shi, H. F. Yang, Z. Li, C. Z. Yu, B. Tu, D. Y. Zhao, *Angew. Chem. Int. Ed.* **2005**, *44*, 7053–7059; *Angew. Chem.* **2005**, *117*, 7215–7221.

[21] Y. F. Zhao, X. Liu, K. X. Yao, L. Zhao, Y. Han, *Chem. Mater.* **2012**, *24*, 4725–4734.

[22] P. J. Herley, W. Jones, *Mater. Lett.* **1983**, *1*, 131–136.

[23] a) S. Chumphongphan, U. Filsø, M. Paskevicius, D. A. Sheppard, T. R. Jensen, C. E. Buckley, *Int. J. Hydrogen Energy* **2014**, *39*, 11103–11109; b) Y. Li, G. Zhou, F. Fang, X. Yu, Q. Zhang, L. Ouyang, M. Zhu, D. Sun, *Acta Mater.* **2011**, *59*, 1829–1838.

[24] E. H. Majzoub, J. L. Herberg, R. Stumpf, S. Spangler, R. S. Maxwell, *J. Alloys Compd.* **2005**, *394*, 265–270.

[25] T. Mueller, G. Ceder, *ACS Nano* **2010**, *4*, 5647–5656.

[26] a) R. K. Bhakta, S. Maharrey, V. Stavila, A. Highley, T. Alam, E. Majzoub, M. Allendorf, *Phys. Chem. Chem. Phys.* **2012**, *14*, 8160–8169; b) Rafi-ud-din, Q. Xuanhui, L. Ping, L. Zhang, M. Ahmad, M. Z. Iqbal, M. Y. Rafique, M. H. Farooq, *RSC Adv.* **2012**, *2*, 4891–4903; c) G. Sandrock, K. Gross, G. Thomas, *J. Alloys Compd.* **2002**, *339*, 299–308.

[27] a) H. E. Kissinger, *Anal. Chem.* **1957**, *29*, 1702–1706; b) C. P. Baldé, B. P. C. Hereijgers, J. H. Bitter, K. P. de Jong, *J. Am. Chem. Soc.* **2008**, *130*, 6761–6765.

[28] a) R. K. Bhakta, J. L. Herberg, B. Jacobs, A. Highley, R. Behrens, N. W. Ockwig, J. A. Greathouse, M. D. Allendorf, *J. Am. Chem. Soc.* **2009**, *131*, 13198–13199; b) X. Fan, X. Xiao, J. Shao, L. Zhang, S. Li, H. Ge, Q. Wang, L. Chen, *Nano Energy* **2013**, *2*, 995–1003; c) T. K. Nielsen, P. Javadian, M. Polanski, F. Besenbacher, J. Bystrzycki, T. R. Jensen, *J. Phys. Chem. C* **2012**, *116*, 21046–21051.

[29] E. H. Majzoub, F. Zhou, V. Ozoliņš, *J. Phys. Chem. C* **2011**, *115*, 2636–2643.

[30] P. A. Berseth, A. G. Harter, R. Zidan, A. Blomqvist, C. M. Araújo, R. H. Scheicher, R. Ahuja, P. Jena, *Nano Lett.* **2009**, *9*, 1501–1505.

[31] a) L. H. Kumar, C. V. Rao, B. Viswanathan, *J. Mater. Chem. A* **2013**, *1*, 3355–3361; b) Meenakshi, D. Agnihotri, H. Sharma, *Comput. Theor. Chem.* **2016**, *1097*, 61–69; c) Y. Cho, S. Li, J. L. Snider, M. A. T. Marple, N. A. Strange, J. D. Sugar, F. El Gabaly, A. Schneemann, S. Kang, M.-h. Kang, H. Park, J. Park, L. F. Wan, H. E. Mason, M. D. Allendorf, B. C. Wood, E. S. Cho, V. Stavila, *ACS Nano* **2021**, *15*, 10163–10174.